Chemical Engineering Journal 459 (2023) 141524

Contents lists available at ScienceDirect

Chemical Engineering Journal

journal homepage: www.elsevier.com/locate/cej

Metal-organic framework nanocrystals enabled efficient and durable two-step perovskite photovoltaics

Xiao Liang [a,b], Kang Zhou [a], Dawei Duan [a], Fei Wang [a,b], Chuangye Ge [a], Xianfang Zhou [a,b], Mingjian Yuan [d], Yumeng Shi [e], Haoran Lin [a], Quanyao Zhu [b], Gang Li [c,f], Hanlin Hu [a,*]

[a] Hoffman Institute of Advanced Materials, Shenzhen Polytechnic, 7098 Liuxian Boulevard, Shenzhen 518055, China
[b] State Key Laboratory of Advanced Technology for Materials Synthesis and Processing, School of Materials Science and Engineering, Wuhan University of Technology, Wuhan 430070, China
[c] Department of Electronic and Information Engineering, Research Institute for Smart Energy (RISE), The Hong Kong Polytechnic University, Hung Hom, Kowloon, Hong Kong, China
[d] Renewable Energy Conversion and Storage Center (RECAST) College of Chemistry, Nankai University, Tianjin 300071, China
[e] International Collaborative Laboratory of 2D Materials for Optoelectronics Science and Technology of Ministry of Education, Institute of Microscale Optoelectronics, Shenzhen University, Shenzhen 518060, China
[f] The Hong Kong Polytechnic University Shenzhen Research Institute, Guangdong, Shenzhen 518057, China

ARTICLE INFO

Keywords:
Two-steps
PbI_2
MOF
GIWAXS
Perovskite solar cells

ABSTRACT

The complete conversion of PbI_2 into high-grade perovskite material with less trap-state density and long-term durability still remains challenging for two-step perovskite photovoltaics. In this work, nanoscale UiO-66, as a classical Zr-MOFs with respectable stability and high specific surface area, has been innovatively introduced into the PbI_2 layer to facilitate the conversion process by morphology tuning and also ultimately improve the durability of the resultant perovskite photovoltaic devices. The added UiO-66 has impressively changed the morphology of PbI_2 film from a pristine compact one into a porous structure, providing better contact with organic salt during second-step deposition, consequently benefitting the thorough and uniform perovskite conversion process. Importantly, the addition of UiO-66 has effectively suppressed the halide vacancies formation due to the increased halide vacancy formation energy at the interface, as evidenced by density functional theory (DFT) calculation, leading to noticeably enhanced charge transport property and greatly improved optoelectronic property. Furthermore, the crystal orbital Hamilton population (COHP) calculation result directly proves that the incorporation of UiO-66 has enhanced the stability of perovskite materials by intensifying the bonding interaction of Pb-I bonds at the interface. Consequently, the UiO-66-assisted devices deliver a champion power conversion efficiency of 23.05% with noticeably improved stability, significantly outperforming the pristine devices. This work demonstrates the brightening potential of MOFs to assist the consequential manufacture of highly efficient and stable perovskite solar cells for upscaling process and deployment in the near future.

1. Introduction

Organic-inorganic halide perovskite solar cells (PSCs), as the front runner among emerging photovoltaic technologies with the record-certified power conversion efficiency (PCE) reached 25.7 % [1], have attracted tremendous research interest [2–11]. At this stage, the scaling-up of PSCs with improved durability is receiving growing attention. In contrast to the one-step method, two-step approaches have been favored to apply to large-area manufacturing of PSCs because of their better crystallization control and higher reproducibility [12,13]. However, the dense and compact PbI_2 film severely hinders the permeation of organic salt solution with the unsatisfactory conversion efficiency of PbI_2 into perovskite film and seriously hampers further development [14–22].

To solve this issue, intensive research efforts have been made to tune the morphology of PbI_2 thin films to enhance the conversion process. Zhao and co-workers first introduced two-dimensional (2D) monolayer $Ti_3C_2T_x$ nanosheets into the PbI_2 layer to form porous channels to enhance the susceptibility of PbI_2. These porous channels effectively reduce the amount of the residual PbI_2 in the perovskite film, promotes the perovskite transformation process, and magnify the grain size of

* Corresponding author.
E-mail addresses: cglamri@whut.edu.cn (Q. Zhu), gang.w.li@polyu.edu.hk (G. Li), hanlinhu@szpt.edu.cn (H. Hu).

https://doi.org/10.1016/j.cej.2023.141524
Received 3 November 2022; Received in revised form 2 January 2023; Accepted 18 January 2023
Available online 20 January 2023

perovskite [23]. A. Alharbi et al. found that the addition of mixtures of 1D δ-$RbPbI_3$ and δ-$CsPbI_3$ into the PbI_2 solution could induce the formation of porous mesostructured PbI_2 films. These porosity channels awfully facilitate the heterogeneous nucleation and the permeation of organic cations within the PbI_2 layer [24]. Zhang and co-workers incorporated molybdenum disulfide nanosheets into the PbI_2 solution, functioning as nano-frameworks to postpone the quick nucleation process of PbI_2 and enlarge the physical volume of the PbI_2 film with a nano-porous channel morphology. Hence, the penetration of the organic cations is remarkably promoted, leading to a perfected surface perovskite crystal orientation with perceptively reduced residual stress and trap state density [25]. To really achieve the application goal of perovskite photovoltaic technology, long-term stability is another challenging issue that draws huge research interest. With impressive chemical and thermal stability, high specific surface area, interconnected porous structure, and solution-processable nanoscale metal–organic framework (MOF) has attracted increasing attention and successfully applied in the perovskite photovoltaic device [9]. In 2015, Huang et al. first reported incorporating MOF crystals into the perovskite photo-active layer to fabricate PSCs. They synthesized the MOF-525 nanocrystals (≈140 nm) and integrated them with perovskite. The microporous structure of nanoscale MOF-525 significantly enhanced the morphology and crystallinity of the perovskite thin film [26]. In 2019, Lee et al. methodically investigated the influence of MOF/perovskite heterojunction on the photovoltaic performance and durability of PSCs with inverted p–i–n structure. They found that the hybrid MOFs were mainly distributed over the perovskite grain boundaries, providing a passivation function of perovskite grain boundaries with noticeably improved device stability [27]. In 2021, Dou et al. introduced the ultrathin Eu-MOF layer between the electron-transport layer and the perovskite absorber to suppress defects and improve the device's stability. They found that the Eu-MOF can reduce disintegration under ultraviolet light and improve light utilization as well as improve the J_{sc} [28]. To give an overview of MOF-assisted perovskite photovoltaic studies, we have systematically summarized the photovoltaic parameters of the MOFs-assisted perovskite heterojunction of PSCs as shown in supporting information (Table S3).

Here, we innovatively introduced nanoscale UiO-66 into the PbI_2 layer for the sequential deposition of perovskite solar cells, which has not been explored and reported so far. It has been found that the addition of UiO-66 has noticeably changed the morphology of PbI_2 thin film into a more porous structure, as confirmed by top-view SEM images. After the second step of organic salt deposition and post thermal annealing, we then systematically examined the conversion process of those PbI_2 thin films with the help of GIWAXS. The 2D GIWAXS data shows that an obvious PbI_2 scattering peak at 0.9 nm^{-1} was presented for the pristine sample, while an almost negligible one for the one modified with UiO-66, indicating a more complete conversion for UiO-66-assisted PbI_2 sample. The incorporation of UiO-66 has enhanced the charge carrier transport properties and improved the opto-electronic properties upon SCLC and different physical measurements. Furthermore, DFT calculation result suggests the addition of UiO-66 has effectively suppressed the halide vacancy formation due to the increased halide vacancy formation energy at the interface. In addition, the crystal orbital Hamilton population (COHP) calculation result demonstrates that the addition of UiO-66 has enhanced the stability of perovskite materials by intensifying the bonding interaction of Pb-I bonds at the interface. Consequently, the UiO-66-assisted devices deliver a champion PCE exceeding 23 % with noticeably improved stability.

2. Results and discussion

Nanoscale UiO-66 has been added into the PbI_2 solution to fabricate UiO-66-assisted PbI_2 thin film during the first deposition step. Detailed information including the morphology, size distribution, and N_2 adsorption–desorption isotherms of UiO-66 crystals are shown in the supporting Information (Figs. S1 and S2). Plan-view morphology of the corresponding PbI_2 thin films was characterized by SEM, as shown in Fig. 1(a-b). It can be clearly noticed that the pristine film consists of densely packed plate-like PbI_2 crystals with few voids (Fig. 1a), while the addition of UiO-66 has changed the morphology of PbI_2 thin films into more deep pin-holes, as shown in Fig. 1b. To better demonstrate this, we further use SEM to record the morphology difference between the two samples with high-magnification as shown in the supporting information (Fig. S5a, b). We measured the root mean square value (Ra) of the PbI_2 surface by atomic force microscopy (AFM) and found that the surface roughness is increased from 5.66 nm of the pristine (Fig. S6a, b) to 6.34 nm of the UiO-66-assisted (Fig. S6d, e). The mean value of vertical height curves vary with distance are recorded in the corresponding AFM image for (Fig. S6c) pristine (−0.0329 nm) and (Fig. S6f) UiO-66-assisted PbI_2 films (−0.437 nm). These results demonstrate that UiO-66-assisted PbI_2 films exhibit a deeper pore structure, providing better contact with organic salt during second-step deposition. Furthermore, the cross-sectional SEM image exhibits a more porous morphology in contrast to the pristine one (Fig. S7). The modified morphology of PbI_2 thin film with pin-holes is supposed to be beneficial for the perovskite conversion process due to the improved contact [29,30]. Grazing-incidence wide-angle X-ray scattering (GIWAXS) has been performed to examine the crystalline quality and crystal structure of PbI_2 thin films. 2D GIWAXS patterns were recorded for both pristine and UiO-66-assisted PbI_2 thin films, as shown in Fig. 1(c, d). The scattering peak located at $q = 0.9$ $Å^{-1}$ is identified as the hexagonal (0 0 1) of PbI_2 as reported previously [31]. According to the radial integration curves from 2D GIWAXS patterns plotted in Fig. 1(e), the pristine and UiO-66-assisted PbI_2 thin films exhibit identical scattering peaks from the hexagonal (0 0 1) of PbI_2. This result suggests the addition of UiO-66 has changed the PbI_2 in terms of morphology rather than the crystal structure or orientation of PbI_2 crystals.

To investigate how the changed morphology of PbI_2 thin films influenced the conversion process to final perovskite films, first, we examined the morphology of the corresponding perovskite thin films morphology after the second-step organic salt deposition followed by post-thermal annealing treatment. Fig. 2 (a,b) are the plan-view SEM images for pristine and UiO-66-assisted perovskite thin film, respectively. The perovskite grain size for each sample has been statistically calculated as the insert indicated. Compared to the average grain size of ca. 454 nm for the pristine sample, the addition of UiO-66 has helped to enlarge the perovskite grain size with an average grain size of ca. 733 nm. The cross-sectional SEM micrographs (Fig. S8) exhibit similar grain size and the thickness of the perovskite film is about 700 nm. This can be understood as the added UiO-66 can retard the nucleation rate at the initial stage, leading to an increased perovskite grain size. Furthermore, we have utilized thermogravimetric analysis (TGA) and SEM-Energy dispersive spectroscopy (EDS) for pristine and UiO-66-assisted one to determine the presence of UiO-66 in the final perovskite films. The TGA results suggest that the decomposition temperatures (T_d, 5 % mass loss; as revealed in Fig. S9) for pristine (272.7 °C) is slightly lower than that of UiO-66-assisted one (279.75 °C) due to the better thermal stability of UiO-66 nano-crystals, although its amount is quite limited. The SEM-EDS mapping of the UiO-66-assisted perovskite film (Fig. S11) confirms that both Zr and O elements can be detected, visualizing the presence of UiO-66 on perovskite film compared with the undetected Zr and O elements of pristine sample (Fig. S10). More importantly, the 2D GIWAXS results suggest that the scattering peak is distinct between the two samples. In contrast to the pristine perovskite film (Fig. 2c), the UiO-66-assisted one exhibits much less intensity for the scattering ring at a low q value of 0.9 $Å^{-1}$ (Fig. 2d), corresponding to (0 0 1) of PbI_2 crystals. It directly proves that the addition of UiO-66 can facilitate the conversion of PbI_2 into perovskite material with almost negligible residuals in the final perovskite film. To quantitatively illustrate this, we have plotted the radial integration curves in Fig. 2(e) from the corresponding 2D GIWAXS patterns. A strong scattering peak at $q = 1.0$ $Å^{-1}$ can be

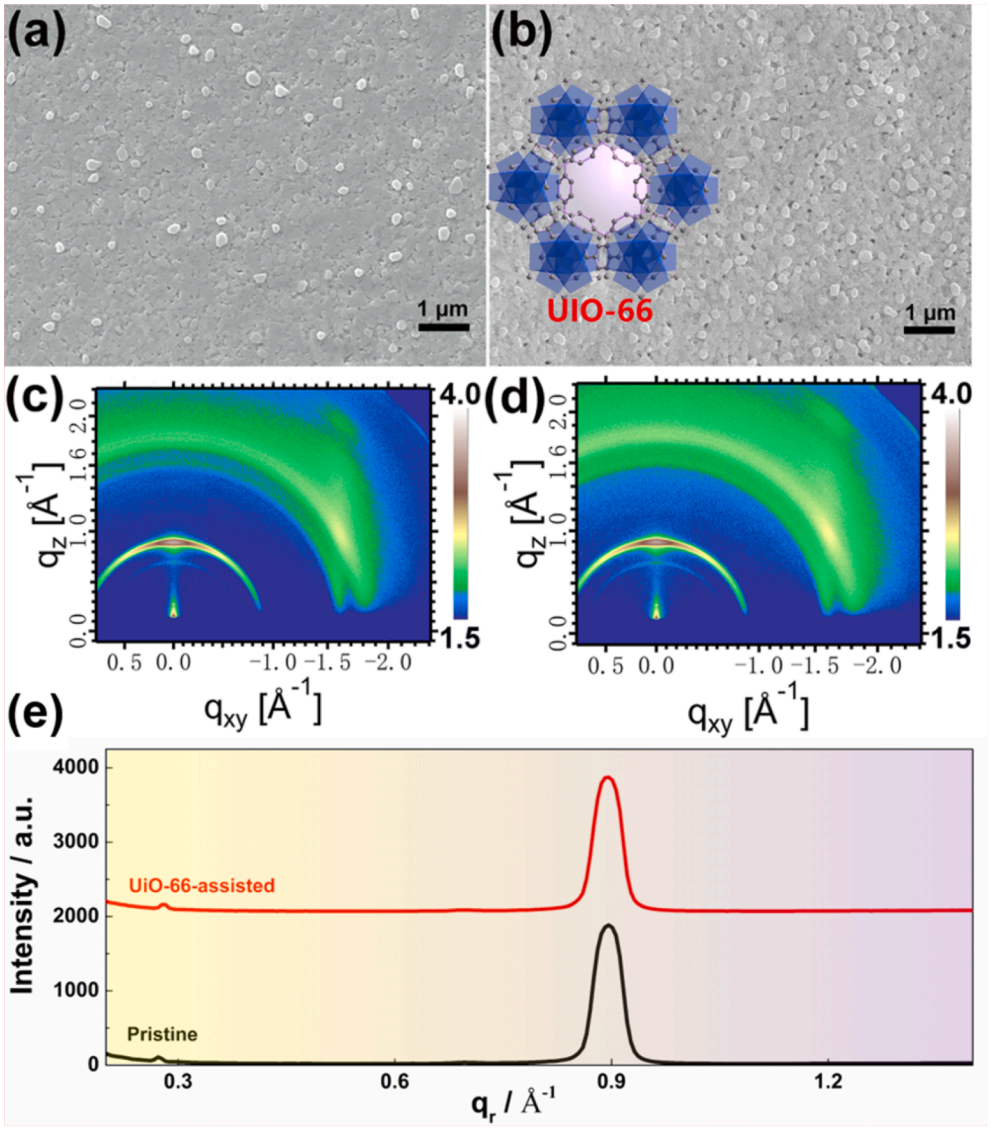

Fig. 1. The plan-view (top) scanning electron microscopy (SEM) images of (a) the pristine and (b) UiO-66-assisted PbI_2 thin films with the crystal structure of UiO-66. The 2D grazing-incidence wide-angle X-ray scattering (GIWAXS) images of (c) pristine and (d) UiO-66-assisted PbI_2 thin film. (e) Radial integration of both pristine and UiO-66-assisted PbI_2 from 2D GIWAXS patterns.

observed for both samples, attributed to the (1 1 0) of perovskite crystals. For the pristine one, a strong scattering peak at $q = 0.9$ Å^{-1} can be clearly noticed next to the scattering peak from (1 1 0) of perovskite crystals, which is due to (0 0 1) of PbI_2 crystals as mentioned above. For the UiO-66-assisted sample, an almost negligible scattering peak shows up at the same location ($q = 0.9$ Å^{-1}) for the UiO-66-assisted sample, indicating few PbI_2 residuals in the final perovskite film. More efficient conversion of PbI_2 into perovskite materials for the UiO-66-assisted one can be understood by the changed PbI_2 morphology with more distributed pin-holes due to the addition of UiO-66, as discussed above. It enables organic salt solution effectively penetrate into the underlying PbI_2 during the second-step deposition and promotes the contact between PbI_2 and organic salt, resulting in the facilitated conversion of PbI_2 into perovskite material.

Crystal structures of pristine and UiO-66-assisted PbI_2 thin films were evaluated by XRD, as shown in Fig. 3(a). Both PbI_2 films show a strong diffraction peak at 12.8°, corresponding to the (0 0 1) lattice plane of crystallized PbI_2 [32]. The UV–vis absorption spectra of the pristine and UiO-66-assisted PbI_2 thin films showed no noticeable change (Fig. 3b). The XRD patterns (Fig. 3c) for both perovskite samples show two prominent diffraction peaks at $2\theta \approx 14.2°$ and 28.6°, attributed to the (1 1 0) and (2 2 0) of the perovskite phase. It is worth mentioning that the intensity of the diffraction peak at 12.80° exhibit a remarkable reduction for UiO-66-assisted perovskite film compared to the pristine one, as shown in Fig. 3c. These XRD results are in good agreement with the 2D GIWAXS data as discussed above. The UV–vis absorption spectra of both perovskite samples are shown in Fig. 3d. Quite similar to the PbI_2, no obvious difference can be noticed for the onset of the two absorption spectra for perovskite samples, indicating that the addition of UiO-66 did not change the optical bandgap of either PbI_2 crystals or perovskite material. Furthermore, in contrast to the pristine one, based on the XPS data, the peaks of Pb 4f and I 3d are both shifted to higher binding energies for UiO-66-assisted PbI_2 film (Fig. S12), indicating the strong electronic interactions between the UiO-66 and Pb^{2+} and I^- [33–35]. To further examine their potential specific interactions between UiO-66 and PbI_2. Fourier transform infrared (FTIR) spectra of films composed of equimolar quantities of UiO-66 and PbI_2 were employed (Fig. S13). For UiO-66, the stretching vibrations of C═O (1656 cm^{-1}), asymmetric stretching of O—C—O (1586 cm^{-1}), symmetric stretching of O—C—O (1398 cm^{-1}), stretching of C—O (1020 cm^{-1}) [36], stretching of Zr—O (746 cm^{-1}) [37], and bend of O—H (665 cm^{-1}) [38] are observed. For films composed of equimolar

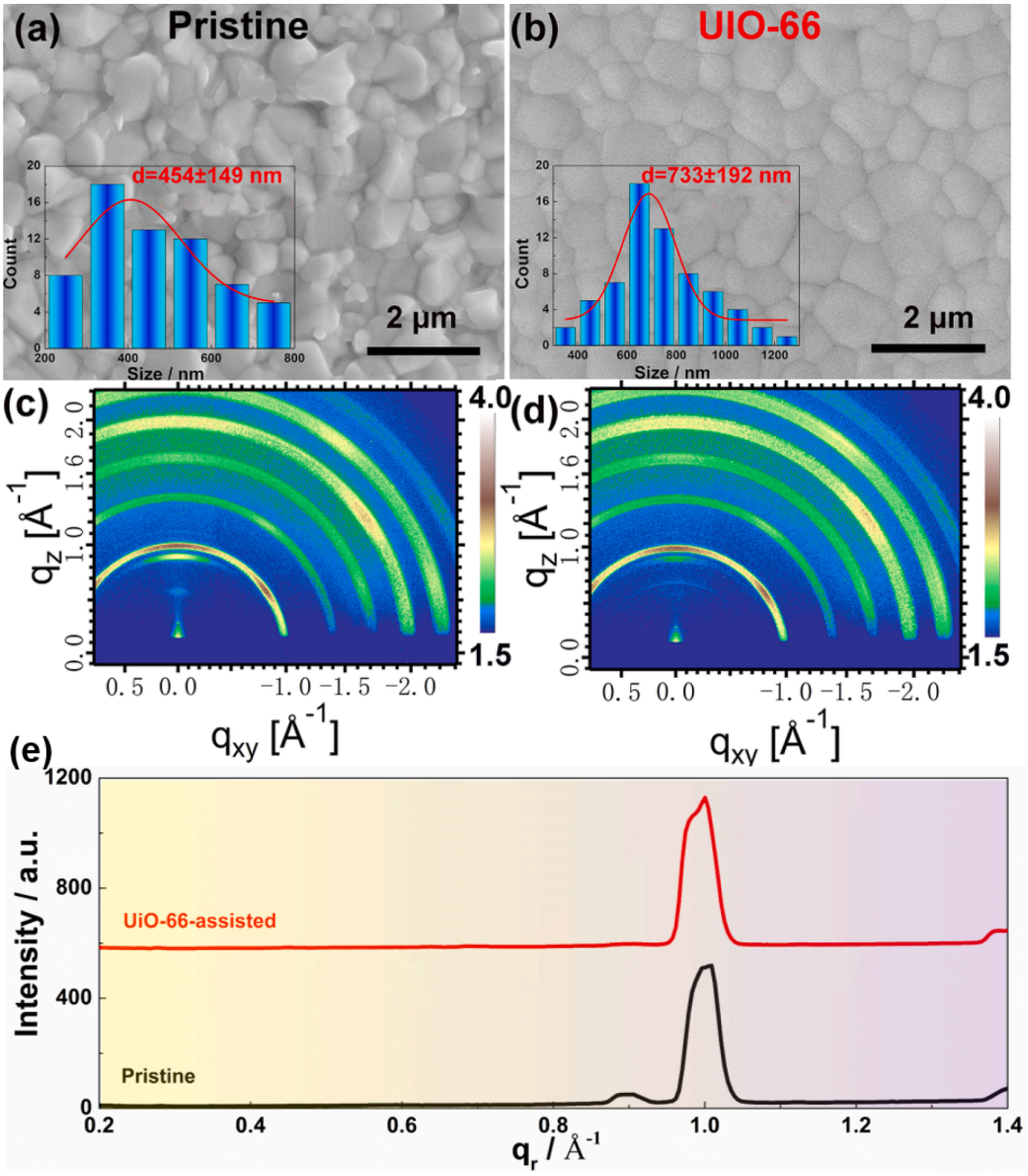

Fig. 2. The plan-view (top) SEM and grain size distribution histograms (inset) of the (a) pristine and (b) UiO-66-assisted perovskite films. 2D GIWAXS images of (c) pristine and (d) UiO-66-assisted perovskite thin film. and (e) Radial integration of both pristine and UiO-66-assisted perovskite from 2D GIWAXS patterns.

quantities of UiO-66 and PbI_2, almost all vibration peaks are obviously shifted to a lower wavenumber, indicating that the strong interaction between O and Pb and H and I [34]. The addition of UiO-66 crystals has improved the PbI_2 conversion into perovskite material, resulting in high-quality perovskite thin film. The time-resolved PL (Fig. 3f) confirms that the UiO-66-assisted perovskite sample shows a significantly increased charge carrier lifetime (t = 326 ns for the pristine while t = 587 ns for the UiO-66-assisted perovskite, as shown in Fig. S14), indicating the higher optoelectronic quality of UiO-66-assisted perovskite thin film and an impressively suppressed non-radiative recombination process [39]. This result is also in good agreement with the steady-state PL with enhanced PL peak intensity for the UiO-66-assisted perovskite sample, as shown in Fig. 3e.

To investigate more in-depth information on how the added UiO-66 affects the perovskite thin film, the DFT calculations using the Vienna Ab initio Simulation Package code have been conducted to reveal the detailed interaction mechanism between UiO-66 crystal and perovskite material. The exposed plane for perovskite and UiO-66 is (0 0 1). The optimized structures and charge density difference of UiO-66/perovskite heterojunctions as shown in Fig. 4(a). The interaction at the interface is dominated by the Pb-C and Zr-O bonds. UiO-66 transfers 0.05 electrons to the perovskite calculated by Bader approach. The formation energies for the iodine vacancy at the interface were calculated to be 3.32 eV, which is higher than the value of 1.82 eV on the surface of $MAPbI_3$. It suggests that the addition of UiO-66 has remarkably stabilized the perovskite materials by suppressing the formation of iodine vacancy at the interface with its porous structure and high specific surface area. Then, we performed the COHP calculations to analyze the stability of the Pb-I bonds (Fig. 4b). COHP partitions the band structure energy into orbital-pair interactions, showing bonding (negative values) and antibonding (positive values) contributions to the band. A plot between energy and -COHP is usually adopted. The COHP reflected the bonding and antibonding interactions in the system. Higher antibonding states at the Fermi level indicate that the system has poorer chemical stability [40]. The integral of COHP (ICOHP) with respect to the energy reflects the bond strength (net bonding contribution). The

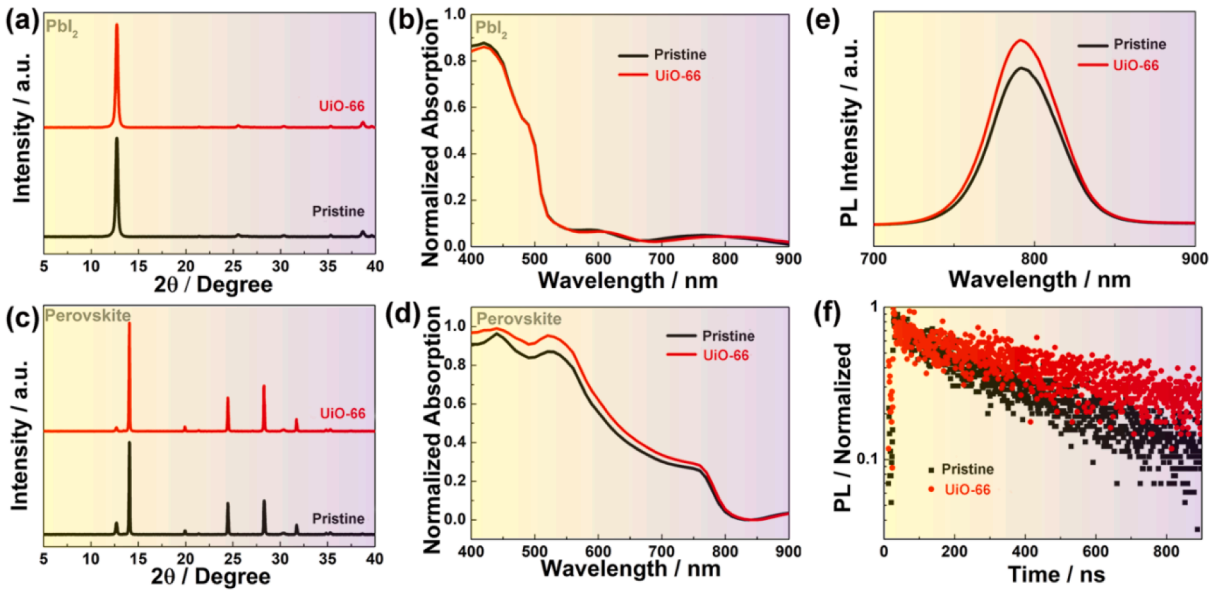

Fig. 3. (a) XRD patterns and (b) UV–vis of the pristine and UiO-66-assisted PbI_2 films. (c) XRD patterns and (d) UV–vis of the pristine and UiO-66-assisted perovskite films. (e) Steady-state photoluminescence (PL) and (f) time-resolved PL (TRPL) spectra of the pristine and UiO-66-assisted perovskite films.

-ICOHP for the Pb-I bonds at the interface between perovskite and UiO-66 turns out to be 1.21 eV, mainly contributed by the bonding states ranging from −5.0 eV to −2.5 eV, which is higher than the value of 1.05 eV for the surface of $MAPbI_3$. Bonding states are mainly located ranging from −5.0 to −2.5 eV, which contributes to stability of the Pb-I bond. This COHP calculation result suggests that the incorporation of UiO-66 has improved the stability of perovskite materials by intensifying the bonding interaction of Pb-I bonds.

Further direct analysis of the perovskite film's trap density (N_t) was conducted using the Space-charge-limited current (SCLC) measurement for hole-only devices comprised of ITO/PEDOT: PSS/perovskite/SpiroOMeTAD/Au, as presented in Fig. 5(a-c). The N_t of UiO-66-assisted perovskite films was calculated using the SCLC method according to the following equation (1) [41].

$$N_t = \frac{2\varepsilon\varepsilon_0 V_{TFL}}{eL^2} \quad (1)$$

Where e denotes elementary charge, L represents the thickness of the perovskite film (≈700 nm), ε means the relative dielectric constant of perovskite [42], and ε_0 indicates the vacuum permittivity (8.8542×10^{-14} F/cm). V_{TFL} is the onset voltage of the trap-filled limit region. The V_{TFL} of the pristine and UiO-66-assisted perovskite films deposited on SnO_2 substrates are 0.72 and 0.25 V. Thus, the calculated N_t is 3.51×10^{15} cm^{-3} for the UiO-66-assisted one, while remarkably higher N_t of 1.01×10^{16} cm^{-3} for the pristine (Fig. 5c). The Mott–Schottky analysis of capacitance versus voltage curves was applied to verify the variation of the built-in potential (V_{bi}) in PSCs based on both pristine and UiO-66-assisted samples (Fig. S15) [43]. The V_{bi} of pristine and UiO-66-assisted device calculated from the intercept of the linear region are 0.93 V and 0.98 V, respectively, indicating that UiO-66-assisted PSCs is favorable to extracting the photogenerated carriers and excellently suppressing the recombination, leading to the enhancement of V_{oc} [44]. Subsequently, the dark current measurements (Fig. S16) of the UiO-66-assisted devices were lower than that of the pristine sample in both the forward and reverse bias regions, indicating that a larger shunt resistance was achieved with UiO-66-assisted [45]. Fig. 5(d) shows the measured EQE_{EL} for devices versus current density in an ambient air environment. The UiO-66-assisted devices exhibit a maximum EQE_{EL} of 7.11 % at a sun (25 mA cm^{-2}). The pristine sample display EQE_{EL} of 4.17 %. The EL intensity for the pristine and UiO-66-assisted devices at biases from the lowest voltage (1.00 V) to the highest voltage (1.35 V). is available in Fig. 5(e, f). The higher bias voltages deliver higher EQE_{EL} as well as higher stationary values due to the higher injected current [46]. It suggests that the UiO-66-assisted device shows much stronger EL intensity with less trap state density.

The PV performance of UiO-66-assisted perovskite thin films is evaluated by incorporating them into PSC devices of the architecture shown in Fig. 6(a). Fig. 6(b) gives a cross-sectional SEM image of the UiO-66-assisted PSCs with a structure of ITO/SnO_2/UiO-66-assisted perovskite/SpiroOMeTAD/Au. Electrochemical impedance spectroscopy (EIS) was also conducted to analyze PSCs' electrical properties and charge recombination behavior [47]. Fig. 6(c) and the inset image display the EIS spectra of the cells without applied bias and sunlight illumination and the equivalent circuit diagram, which consists of the series resistance (R_s), recombination resistance (R_{rec}), and capacitance (CPE_{rec}) [48]. The value of R_{rec} is a standard parameter for evaluating the charge recombination behavior in PSCs, and the higher R_{rec} represents that charge recombination is harder [49,50]. The R_{rec} value of UiO-66-assisted cells was 244 kΩ more than the pristine (167 kΩ). It indicated that the recombination of charge carriers was strongly suppressed in the UiO-66-assisted PSCs. The fitting parameters are listed in Table S4.

Fig. 6(d) shows the pristine's indoor *J–V* curves and UiO-66-assisted PSCs under AM 1.5G illumination at 100 mW cm^{-2}. The UiO-66-assisted device displays a higher striking PCE of 23.05 % (with open-circuit voltage (V_{oc}) of 1.190 V, short-circuit current density (J_{sc}) of 24.16 mA cm^{-2}, and a fill factor (FF) of 80.19 %), demonstrating noticeable improvement in comparison with the PCE of 20.83 % for the pristine device. The UiO-66-assisted device exhibited almost negligible hysteresis as shown in the forward and reverse scanning *J–V* curves (Fig. S17). The improvement of the V_{oc} in the PSCs is reported to be related to the reduced trap-state density and nonradiative recombination losses [51]. The improvement of the FF in the PSCs is likely related to the higher crystallinity of perovskite [45]. Fig. 6e and Fig. S18 reveals that the integrated J_{sc} values (22.77 mA cm^{-2} for pristine and 23.05 mA cm^{-2} for the UiO-66-assisted device) from the external quantum efficiency (EQE) spectra are in good consistency with the J_{sc} extracted from *J-V* curves. The statistical distributions of photovoltaic parameters of pristine and UiO-66-assisted devices are shown in Fig. S19. The UiO-66-assisted devices deliver better repeatability with a tighter distribution and higher average PCE than the pristine devices. The maximum power

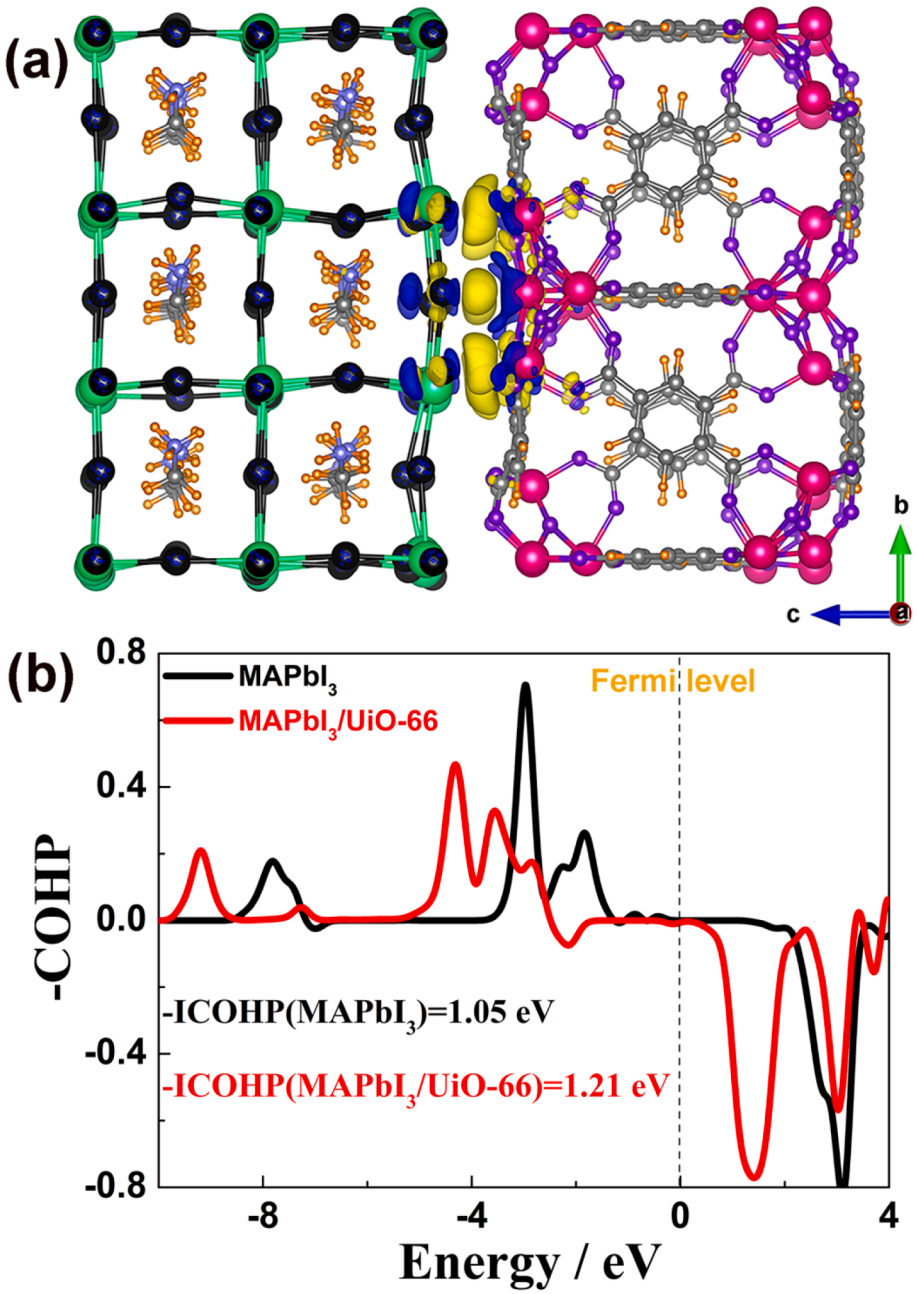

Fig. 4. (a) The charge density difference of $MAPbI_3$/UiO-66. Charge transfer mainly occurs between the I and Zr atoms. Yellow and blue colors label charge accumulation and depletion, respectively. The isovalue for the isosurface is set to 0.002 electrons/bohr^3. (b) The crystal orbital Hamilton population (COHP) illustrated the stability of Pb-I bonds, where the negative values (-COHP) represent antibonding interactions (down side), while positive values represent bonding ones (upper side), and zero represent fermi level. (For interpretation of the references to colour in this figure legend, the reader is referred to the web version of this article.)

point (MPP) tracking under AM 1.5G illumination for the best device, shown in Fig. S20, indicated a stabilized PCE of 20.04 % and 22.70 % for pristine and UiO-66-assisted PSCs at 300 s. Moreover, upon exposure to the dry ambient conditions (RH = 10 %) in the dark, the PCE of the UiO-66-assisted unencapsulated device dropped slowly and maintained 75 % of the initial efficiency after 2000 h, while the pristine device showed quicker degradation and led to a more significant decrease in the efficiency as shown in Fig. 6f. We further investigated the long-term stability of pristine and UiO-66-assisted devices under air ambient conditions and continous white LED illumination in an N_2 atmosphere near the maximum power point. The unencapsulated device presented excellent stability that retained 84 % of its original PCE for over 400 h under air ambient conditions (RH = 40 ± 5 %, T = 21℃), as shown in Fig. S21. More importantly, we performed MPP tracking of devices using a 1-sun equivalent illumination white LED in an N_2 atmosphere. The UiO-66-assisted devices maintained about 81 % of the initial PCE (Fig. S22) under MPP and 1-sun equivalent illumination for 400 h. In contrast, the pristine sample retains 46 % of its initial efficiency over the same time.

3. Conclusion

In summary, we innovatively introduced nanoscale UiO-66 crystals into the PbI_2 layer as a multifunctional additive to fabricate efficient and durable two-step perovskite solar cells. The added UiO-66 has impressively changed the morphology of PbI_2 film into a porous structure, leading to a more efficient perovskite conversion with improved device performance. Importantly, the DFT calculation data proves that the addition of UiO-66 crystals has effectively suppressed the halide vacancy formation due to the increased halide vacancy formation energy at the interface. Furthermore, the COHP calculation result directly evidences that the addition of UiO-66 crystals has intensified the bonding interaction of Pb-I bonds at the interface, resulting in enhanced stability of perovskite materials with fewer halide vacancies and suppressed ion-

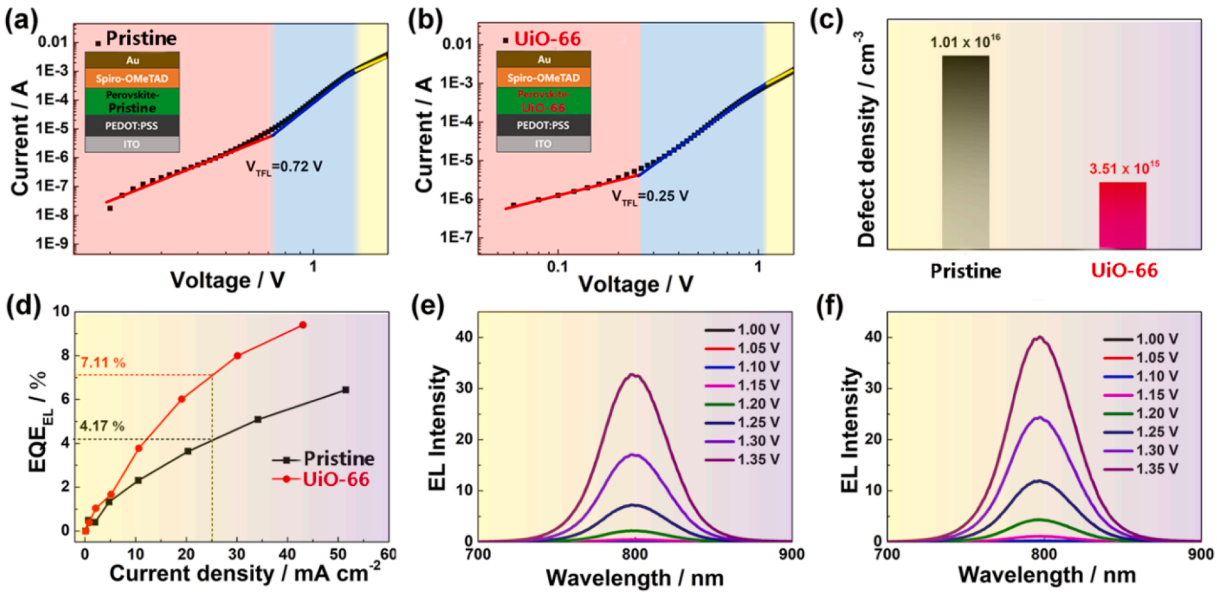

Fig. 5. Space-Charge Limited Current indicates the trap-filling limited voltage (V_{TFL}) of the hole-only devices for (a) pristine, (b) UiO-66-assisted, (c) trap density (N_t) of the PSCs for pristine, and UiO-66-assisted. (d) EQE_{EL} of the PSCs based on pristine and UiO-66-assisted versus current density. EL transients at different bias voltages were observed for (e) pristine and (f) UiO-66.

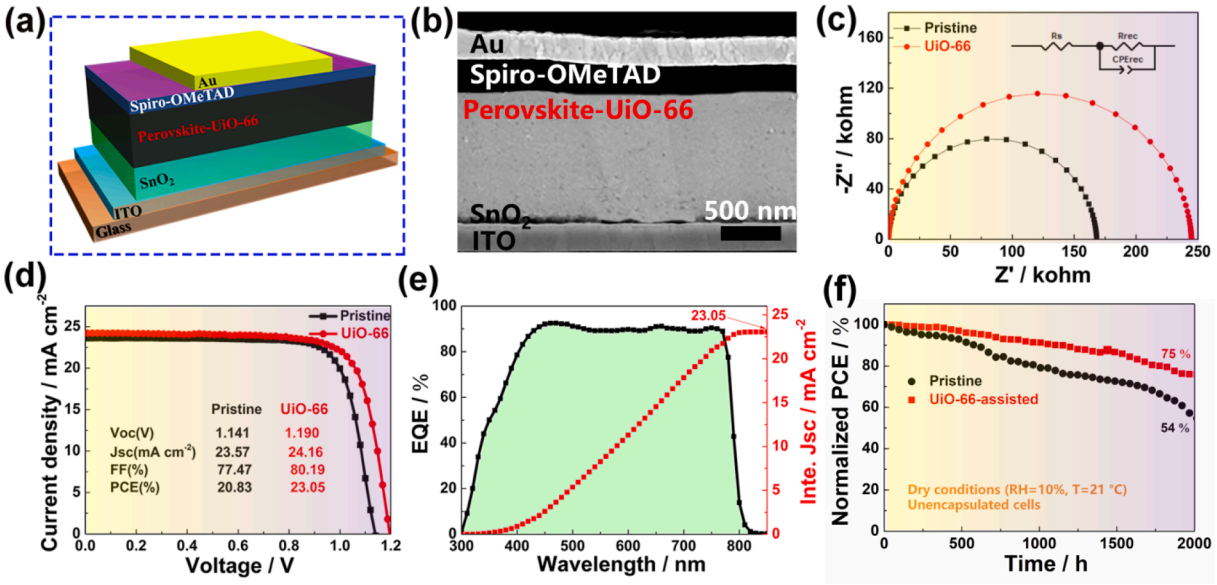

Fig. 6. (a) Device structure of the PSCs with ITO/SnO_2/perovskite/SpiroOMeTAD/Au. (b) The cross-sectional SEM image of the UiO-66-assisted PSC. (c) Nyquist plots for PSCs based on the pristine and UiO-66-assisted without applied bias and sunlight illumination. (d) Current density–voltage (*J-V*) curves of the pristine and UiO-66-assisted devices. (e) Wavelength-dependent EQE spectra and integrated Jsc of the UiO-66-assisted PSCs. (f) The stability study shows normalized PCEs of the pristine and UiO-66-assisted devices unencapsulation over 2000 h in dry conditions (RH = 10 %).

migration. As a result, the UiO-66-assisted devices deliver a champion power conversion efficiency of 23.05 % with noticeably improved stability, significantly outperforming the pristine devices. This work demonstrates the promising potential of MOFs to assist the two-step fabrication of efficient and durable perovskite photovoltaics for upscaling process and deployment in the near future.

Declaration of Competing Interest

The authors declare that they have no known competing financial interests or personal relationships that could have appeared to influence the work reported in this paper.

Data availability

The authors do not have permission to share data.

Acknowledgements

This work is supported by the Scientific Research Startup Fund for Shenzhen High-Caliber Personnel of Shenzhen Polytechnic, No. 6022310038k and 6022310049k. The financial support from the National Natural Science Foundation of China (No. 62004129); Shenzhen Science and Technology Innovation Commission (Project No. JCYJ20200109105003940); Research Grants Council of Hong Kong (GRF grant 15221320, CRF C5037-18G, C7018-20G); the Hong Kong

Polytechnic University funds (Sir Sze-yuen Chung Endowed Professorship Fund (8-8480), and RISE (Q-CDA5)) is gratefully acknowledged.

Appendix A. Supplementary data

Supplementary data (Experimental details, supporting tables and figures. including the SEM images, XRD, BET, XPS spectra, TRPL fit result, Mott–Schottky plots, Dark current, statistical photovoltaic parameters) to this article can be found online at https://doi.org/10.1016/j.cej.2023.141524.

References

[1] NREL, Best Research-Cell Efficiencies: Rev. 19-01-2022, Best Res. Effic. Chart | Photovolt. Res. | NREL. (2022) https://www.nrel.gov/pv/cell-efficiency.html.

[2] Z. Bi, X. Xu, X. Chen, Y. Zhu, C. Liu, H. Yu, Y. Zheng, P.A. Troshin, A. Guerrero, G. Xu, High-performance large-area blade-coated perovskite solar cells with low ohmic loss for low lighting indoor applications, Chem. Eng. J. 446 (2022), 137164, https://doi.org/10.1016/j.cej.2022.137164.

[3] Y. Yang, T. Zhao, M.-H. Li, X. Wu, M. Han, S.-C. Yang, Q. Xu, L. Xian, X. Chi, N.-J. Zhao, H. Cui, S. Li, J.-S. Hu, B. Zhang, Y. Jiang, Passivation of positively charged cationic defects in perovskite with nitrogen-donor crown ether enabling efficient perovskite solar cells, Chem. Eng. J. 451 (2023), 138962, https://doi.org/10.1016/j.cej.2022.138962.

[4] J. Dai, J. Xiong, N. Liu, Z. He, Y. Zhang, S. Zhan, B. Fan, W. Liu, X. Huang, X. Hu, D. Wang, Y. Huang, Z. Zhang, J. Zhang, Synergistic dual-interface modification strategy for highly reproducible and efficient PTAA-based inverted perovskite solar cells, Chem. Eng. J. 453 (2023), 139988, https://doi.org/10.1016/j.cej.2022.139988.

[5] J. Cha, M.K. Kim, W. Lee, H. Jin, H. Na, D. Cung Tien Nguyen, S.-H. Lee, J. Lim, M. Kim, Perovskite nanowires as defect passivators and charge transport networks for efficient and stable perovskite solar cells, Chem. Eng. J. 451 (2023) 138920. https://doi.org/10.1016/j.cej.2022.138920.

[6] J. Peng, F. Kremer, D. Walter, Y. Wu, Y.i. Ji, J. Xiang, W. Liu, T. Duong, H. Shen, T. Lu, F. Brink, D. Zhong, L.i. Li, O. Lee Cheong Lem, Y. Liu, K.J. Weber, T.P. White, K.R. Catchpole, Centimetre-scale perovskite solar cells with fill factors of more than 86 per cent, Nature. 601 (7894) (2022) 573–578.

[7] R. Azmi, E. Ugur, A. Seitkhan, F. Aljamaan, A.S. Subbiah, J. Liu, G.T. Harrison, M. I. Nugraha, M.K. Eswaran, M. Babics, Y. Chen, F. Xu, T.G. Allen, A.u. Rehman, C.-L. Wang, T.D. Anthopoulos, U. Schwingenschlögl, M. De Bastiani, E. Aydin, S. De Wolf, Damp heat–stable perovskite solar cells with tailored-dimensionality 2D/3D heterojunctions, Science. 376 (6588) (2022) 73–77.

[8] M.A. Mahmud, T. Duong, J. Peng, Y. Wu, H. Shen, D. Walter, H.T. Nguyen, N. Mozaffari, G.D. Tabi, K.R. Catchpole, K.J. Weber, T.P. White, Origin of efficiency and stability enhancement in high-performing mixed dimensional 2D–3D perovskite solar cells: A review, Adv. Funct. Mater. 32 (2022) 2009164, https://doi.org/10.1002/adfm.202009164.

[9] X. Liang, X. Zhou, C. Ge, H. Lin, S. Satapathi, Q. Zhu, H. Hu, Advance and prospect of metal-organic frameworks for perovskite photovoltaic devices, Org. Electron. 106 (2022), 106546, https://doi.org/10.1016/j.orgel.2022.106546.

[10] S. Xu, L. Zhang, B. Liu, Z. Liang, H. Xu, H. Zhang, J. Ye, H. Ma, G. Liu, X. Pan, Constructing of superhydrophobic and intact crystal terminal: Interface sealing strategy for stable perovskite solar cells with efficiency over 23%, Chem. Eng. J. 453 (2023), 139808 https://doi.org/10.1016/j.cej.2022.139808.

[11] L. Zhang, G. Qi, Y. Zhang, H. Wu, X. Xu, G. Zhou, H. Zhu, X. Li, G. Wu, H. Chen, Intermolecular interaction assisted fabrication of Dion-Jacobson perovskite film with promoted photovoltaic property, Chem. Eng. J. 451 (2023), 138654, https://doi.org/10.1016/j.cej.2022.138654.

[12] F. Guo, W. He, S. Qiu, C. Wang, X. Liu, K. Forberich, C.J. Brabec, Y. Mai, Sequential deposition of high-quality photovoltaic perovskite layers via scalable printing methods, Adv. Funct. Mater. 29 (2019) 1900964, https://doi.org/10.1002/adfm.201900964.

[13] S. Shahbazi, M.-Y. Li, A. Fathi, E.-W.-G. Diau, Realizing a cosolvent system for stable tin-based perovskite solar cells using a two-step deposition approach, ACS Energy Lett. 5 (2020) 2508–2511, https://doi.org/10.1021/acsenergylett.0c01190.

[14] J. Li, L. Zuo, H. Wu, B. Niu, S. Shan, G. Wu, H. Chen, Universal bottom contact modification with diverse 2D spacers for high-performance inverted perovskite solar cells, Adv. Funct. Mater. 31 (2021) 2104036, https://doi.org/10.1002/adfm.202104036.

[15] X. Lian, L. Zuo, B. Chen, B. Li, H. Wu, S. Shan, G. Wu, X. Yu, Q. Chen, L. Chen, D. Yang, D. Cahen, H. Chen, Light-induced beneficial ion accumulation for high-performance quasi-2D perovskite solar cells, Energy Environ. Sci. 15 (2022) 2499–2507, https://doi.org/10.1039/D2EE01097F.

[16] Z. Xu, Y. Gong, J. Wang, Z. Ma, R. Yu, J. Yang, Y. Liu, Q. Guo, E. Zhou, Z. Tan, Carbon nanofibers fabricated via electrospinning to guide crystalline orientation for stable perovskite solar cells with efficiency over 24%, Chem. Eng. J. 453 (2023), 139961 https://doi.org/10.1016/j.cej.2022.139961.

[17] M. Du, X. Zhu, L. Wang, H. Wang, J. Feng, X. Jiang, Y. Cao, Y. Sun, L. Duan, Y. Jiao, K. Wang, X. Ren, Z. Yan, S. Pang, S. (Frank) Liu,, High-pressure nitrogen-extraction and effective passivation to attain highest large-area perovskite solar module efficiency, Adv. Mater. 32 (2020) 2004979, https://doi.org/10.1002/adma.202004979.

[18] G. Tumen-Ulzii, C. Qin, D. Klotz, M.R. Leyden, P. Wang, M. Auffray, T. Fujihara, T. Matsushima, J. Lee, S. Lee, Y. Yang, C. Adachi, Detrimental effect of unreacted PbI_2 on the long-term stability of perovskite solar cells, Adv. Mater. 32 (2020) 1905035, https://doi.org/10.1002/adma.201905035.

[19] L. Duan, L. Li, Y. Zhao, G. Cao, X. Niu, H. Zhou, Y. Bai, Q. Chen, In-situ interfacial passivation for stable perovskite solar cells, Front. Mater. 6 (2019), https://doi.org/10.3389/fmats.2019.00200.

[20] F. Wang, P. Wai-Keung Fong, Z. Ren, H.-L. Xia, K. Zhou, K. Wang, J. Zhu, X. Huang, X.-Y. Liu, H. Wang, Y. Shi, H. Lin, Q. Zhu, G. Li, H. Hu, In-depth understanding of ionic liquid assisted perovskite film formation mechanism for two-step perovskite photovoltaics, J. Energy Chem. 73 (2022) 599–606, https://doi.org/10.1016/j.jechem.2022.06.040.

[21] H. Hu, M. Qin, P.W.K. Fong, Z. Ren, X. Wan, M. Singh, C. Su, U. Jeng, L. Li, J. Zhu, M. Yuan, X. Lu, C. Chu, G. Li, Perovskite quantum wells formation mechanism for stable efficient perovskite photovoltaics—A real-time phase-transition study, Adv. Mater. 33 (2021) 2006238, https://doi.org/10.1002/adma.202006238.

[22] X. Liang, D. Duan, M.B. Al-Handawi, F. Wang, X. Zhou, C.-y. Ge, H. Lin, Q. Zhu, L. Li, P. Naumov, H. Hu, The Role of Ionic Liquids in Performance Enhancement of Two-Step Perovskite Photovoltaics, Sol. RRL. 7 (1) (2023) 2200856.

[23] Y. Zhao, X. Zhang, X. Han, C. Hou, H. Wang, J. Qi, Y. Li, Q. Zhang, Tuning the reactivity of PbI_2 film via monolayer $Ti_3C_2T_x$ MXene for two-step-processed $CH_3NH_3PbI_3$ solar cells, Chem. Eng. J. 417 (2021), 127912, https://doi.org/10.1016/j.cej.2020.127912.

[24] E.A. Alharbi, T.P. Baumeler, A. Krishna, A.Y. Alyamani, F.T. Eickemeyer, O. Ouellette, L. Pan, F.S. Alghamdi, Z. Wang, M.H. Alotaibi, B. Yang, M. Almalki, M.D. Mensi, H. Albrithen, A. Albadri, A. Hagfeldt, S.M. Zakeeruddin, M. Grätzel, Formation of high-performance multi-cation halide perovskites photovoltaics by δ-$CsPbI_3$/δ-$RbPbI_3$ seed-assisted heterogeneous nucleation, Adv. Energy Mater. 11 (2021) 2003785, https://doi.org/10.1002/aenm.202003785.

[25] Z. Zhang, J. Wang, L. Lang, Y. Dong, J. Liang, Y. Zheng, X. Wu, C. Tian, Y. Huang, Z. Zhou, Y. Yang, L. Wang, L. Kong, C.-C. Chen, Size-tunable MoS_2 nanosheets for controlling the crystal morphology and residual stress in sequentially deposited perovskite solar cells with over 22.5% efficiency, J. Mater. Chem. A. 10 (2022) 3605–3617, https://doi.org/10.1039/D1TA10314H.

[26] T.-H. Chang, C.-W. Kung, H.-W. Chen, T.-Y. Huang, S.-Y. Kao, H.-C. Lu, M.-H. Lee, K.M. Boopathi, C.-W. Chu, K.-C. Ho, Planar heterojunction perovskite solar cells incorporating metal-organic framework nanocrystals, Adv. Mater. 27 (2015) 7229–7235, https://doi.org/10.1002/adma.201502537.

[27] C.-C. Lee, C.-I. Chen, Y.-T. Liao, K.-C.-W. Wu, C.-C. Chueh, Enhancing efficiency and stability of photovoltaic cells by using perovskite/Zr-MOF heterojunction including bilayer and hybrid structures, Adv. Sci. 6 (2019) 1801715, https://doi.org/10.1002/advs.201801715.

[28] J. Dou, C. Zhu, H. Wang, Y. Han, S. Ma, X. Niu, N. Li, C. Shi, Z. Qiu, H. Zhou, Y. Bai, Q. Chen, Synergistic effects of Eu-MOF on perovskite solar cells with improved stability, Adv. Mater. 33 (2021) 2102947, https://doi.org/10.1002/adma.202102947.

[29] X. Xu, M. Li, Y.-M. Xie, Y. Ma, C. Ma, Y. Cheng, C.-S. Lee, S.-W. Tsang, Porous and intercrossed PbI_2–CsI nanorod scaffold for inverted planar FA–Cs mixed-cation perovskite solar cells, ACS Appl. Mater. Interfaces. 11 (2019) 6126–6135, https://doi.org/10.1021/acsami.8b20933.

[30] M.F. Mohamad Noh, N.A. Arzaee, I.N. Nawas Mumthas, A. Aadenan, H. Alessa, M. N. Alghamdi, H. Moria, N.A. Mohamed, A.R. Bin Mohd Yusoff, M.A. Mat Teridi, Facile tuning of PbI_2 porosity via additive engineering for humid air processable perovskite solar cells, Electrochim. Acta. 402 (2022) 139530. https://doi.org/10.1016/j.electacta.2021.139530.

[31] Y. Li, W. Xu, N. Mussakhanuly, Y. Cho, J. Bing, J. Zheng, S. Tang, Y. Liu, G. Shi, Z. Liu, Q. Zhang, J.R. Durrant, W. Ma, A.W.Y. Ho-Baillie, S. Huang, Homologous bromides treatment for improving the open-circuit voltage of perovskite solar cells, Adv. Mater. 34 (6) (2022) 2106280.

[32] N. Cheng, P. Liu, S. Bai, Z. Yu, W. Liu, S.-S. Guo, X.-Z. Zhao, Enhanced performance in hole transport material free perovskite solar cells via morphology control of PbI_2 film by solvent treatment, J. Power Sources. 319 (2016) 111–115, https://doi.org/10.1016/j.jpowsour.2016.04.062.

[33] M. Liu, G. Zhong, Y. Yin, J. Miao, K. Li, C. Wang, X. Xu, C. Shen, H. Meng, Aluminum-doped cesium lead bromide perovskite nanocrystals with stable blue photoluminescence used for display backlight, Adv. Sci. 4 (2017) 1–8, https://doi.org/10.1002/advs.201700335.

[34] Y. Cai, J. Cui, M. Chen, M. Zhang, Y. Han, F. Qian, H. Zhao, S. Yang, Z. Yang, H. Bian, T. Wang, K. Guo, M. Cai, S. Dai, Z. Liu, S. (Frank) Liu, Multifunctional enhancement for highly stable and efficient perovskite solar cells, Adv. Funct. Mater. 31 (2021) 2005776, https://doi.org/10.1002/adfm.202005776.

[35] J. Chen, X. Zhao, S. Kim, N. Park, Multifunctional chemical linker imidazoleacetic acid hydrochloride for 21% efficient and stable planar perovskite solar cells, Adv. Mater. 31 (2019) 1902902, https://doi.org/10.1002/adma.201902902.

[36] F. Ahmadijokani, S. Ahmadipouya, H. Molavi, M. Rezakazemi, T.M. Aminabhavi, M. Arjmand, Impact of scale, activation solvents, and aged conditions on gas adsorption properties of UiO-66, J. Environ. Manage. 274 (2020), 111155, https://doi.org/10.1016/j.jenvman.2020.111155.

[37] Y. Wang, Q. Liao, J. Chen, W. Huang, X. Zhuang, Y. Tang, B. Li, X. Yao, X. Feng, X. Zhang, M. Su, Z. He, T.J. Marks, A. Facchetti, X. Guo, Teaching an old anchoring group new tricks: enabling low-cost, eco-friendly hole-transporting materials for efficient and stable perovskite solar cells, J. Am. Chem. Soc. 142 (2020) 16632–16643, https://doi.org/10.1021/jacs.0c06373.

[38] M. Nasrabadi, M.A. Ghasemzadeh, M.R. Zand Monfared, The preparation and characterization of UiO-66 metal–organic frameworks for the delivery of the drug ciprofloxacin and an evaluation of their antibacterial activities, New J. Chem. 43 (2019) 16033–16040, https://doi.org/10.1039/C9NJ03216A.
[39] P. Hang, J. Xie, C. Kan, B. Li, Y. Zhang, P. Gao, D. Yang, X. Yu, Stabilizing fullerene for burn-in-free and stable perovskite solar cells under ultraviolet preconditioning and light soaking, Adv. Mater. 33 (2021) 2006910, https://doi.org/10.1002/adma.202006910.
[40] J.-J. Wang, Y.-Z. Xu, R. Mazzarello, M. Wuttig, W. Zhang, A review on disorder-driven metal-insulator transition in crystalline vacancy-rich GeSbTe phase-change materials, Materials (Basel). 10 (2017) 862, https://doi.org/10.3390/ma10080862.
[41] R.H. Bube, Trap density determination by space-charge-limited currents, J. Appl. Phys. 33 (1962) 1733–1737, https://doi.org/10.1063/1.1728818.
[42] D. Barrit, P. Cheng, K. Darabi, M.-C. Tang, D.-M. Smilgies, S.(. Liu, T. D. Anthopoulos, K. Zhao, A. Amassian, Room-temperature partial conversion of α-$FAPbI_3$ perovskite phase via PbI_2 solvation enables high-performance solar cells, Adv. Funct. Mater. 30 (11) (2020) 1907442.
[43] S. Li, J. Liu, S. Liu, D. Zhang, C. Liu, D. Li, J. Qi, Y. Hu, A. Mei, H. Han, Yttrium-doped Sn_3O_4 two-dimensional electron transport material for perovskite solar cells with efficiency over 23%, EcoMat. 4 (2022) https://doi.org/10.1002/eom2.12202.
[44] C.-L. Mai, Q. Xiong, X. Li, J.-Y. Chen, J.-Y. Chen, C.-C. Chen, J. Xu, C. Liu, C.-Y. Yeh, P. Gao, Thermally stable D 2h symmetric donor-π-donor porphyrins as hole-transporting materials for perovskite solar cells, Angew. Chemie. 134 (39) (2022), https://doi.org/10.1002/ange.202209365.
[45] H. Li, J. Zhou, L. Tan, M. Li, C. Jiang, S. Wang, X. Zhao, Y. Liu, Y. Zhang, Y. Ye, W. Tress, C. Yi, Sequential vacuum-evaporated perovskite solar cells with more than 24% efficiency, Sci. Adv. 8 (2022), https://doi.org/10.1126/sciadv.abo7422.
[46] M. Córdoba, W. Herrera, A. Koffman-Frischknecht, N. Correa, M.D. Perez, K. Taretto, Electroluminescence transients and correlation with steady-state solar output in solution-prepared $CH_3NH_3PbI_3$ perovskite solar cells using different contact materials, J. Phys. D. Appl. Phys. 53 (2020) 115501. https://doi.org/10.1088/1361-6463/ab60ec.
[47] J. Zhang, Y. Fang, W. Zhao, R. Han, J. Wen, S. (Frank) Liu, Molten-salt-assisted $CsPbI_3$ perovskite crystallization for nearly 20%-efficiency solar cells, Adv. Mater. 33 (2021) 2103770, https://doi.org/10.1002/adma.202103770.
[48] X. Yang, Y. Chen, P. Liu, H. Xiang, W. Wang, R. Ran, W. Zhou, Z. Shao, Simultaneous power conversion efficiency and stability enhancement of $Cs_2AgBiBr_6$ lead-free inorganic perovskite solar cell through adopting a multifunctional dye interlayer, Adv. Funct. Mater. 30 (2020) 2001557, https://doi.org/10.1002/adfm.202001557.
[49] Q. Yao, Q. Xue, Z. Li, K. Zhang, T. Zhang, N. Li, S. Yang, C.J. Brabec, H. Yip, Y. Cao, Graded 2D/3D perovskite heterostructure for efficient and operationally stable MA-free perovskite solar cells, Adv. Mater. 32 (2020) 2000571, https://doi.org/10.1002/adma.202000571.
[50] H. Zhu, Z. Shen, L. Pan, J. Han, F.T. Eickemeyer, Y. Ren, X. Li, S. Wang, H. Liu, X. Dong, S.M. Zakeeruddin, A. Hagfeldt, Y. Liu, M. Grätzel, Low-cost dopant additive-free hole-transporting material for a robust perovskite solar cell with efficiency exceeding 21%, ACS Energy Lett. 6 (2021) 208–215, https://doi.org/10.1021/acsenergylett.0c02210.
[51] H. Wang, Z. Wang, Z. Yang, Y. Xu, Y. Ding, L. Tan, C. Yi, Z. Zhang, K. Meng, G. Chen, Y. Zhao, Y. Luo, X. Zhang, A. Hagfeldt, J. Luo, Ligand-modulated excess PbI_2 nanosheets for highly efficient and stable perovskite solar cells, Adv. Mater. 32 (2020) 2000865, https://doi.org/10.1002/adma.202000865.